Contents lists available at ScienceDirect

Physica D

Measures of order for nearly hexagonal lattices

Francis C. Motta [a],*, Rachel Neville [b], Patrick D. Shipman [b], Daniel A. Pearson [c],
R. Mark Bradley [c]

[a] *Duke University Math Department, 120 Science Drive, Rm 117 Physics Bldg, Durham, NC 27708-0320, USA*
[b] *Department of Mathematics, Colorado State University, 1874 Campus Delivery, Fort Collins, CO 80523-1874, USA*
[c] *Department of Physics, Colorado State University, 1875 Campus Delivery, Fort Collins, CO 80523-1875, USA*

HIGHLIGHTS

- Novel topological measures of order for nearly hexagonal lattices are introduced.
- The topological measures are more sensitive and stable than traditional gauges.
- The measures provide insight into nanoscale patterns produced by ion sputtering.
- Patterning a surface before sputtering can lead to much improved hexagonal order.

ARTICLE INFO

ABSTRACT

Motivated by hexagonal patterns with defects in natural and laboratory systems, we compare quantitative measures of order for nearly hexagonal, planar lattices. These include a spectral measure of order based on the Fourier transform, a geometric measure of order using the Delaunay triangulation, and topological measures of order introduced in this paper. The topological measures are based on a tool from topological data analysis called persistent homology. We contrast these measures of order by comparing their sensitivity to perturbations of Bravais lattices. We then study the imperfect hexagonal arrangements of nanodots produced by numerical simulations of partial differential equations that model the surface of a binary alloy undergoing erosion by a broad ion beam. These numerical experiments further distinguish the various measures of hexagonal order and highlight the role of various model parameters in the formation and elimination of defects. Finally, we quantify the dependence of order on prepatterning the surface to suggest experimental protocols that could lead to improved order in nanodot arrays.

© 2018 Elsevier B.V. All rights reserved.

1. Introduction

A variety of natural systems and laboratory experiments can give rise to patterns. Hexagonal lattices patterns are found, for example, in Rayleigh–Bénard convection experiments [1], the Rosensweig instability in ferrofluids [2], and nanoscale structures formed by bombarding a binary material by a broad ion beam [3–6]. These patterns are seldom perfect hexagonal lattices. Defects, such as penta–hepta pairs or grain boundaries between regions in which the lattices have different orientations, are common.

The order in a surface pattern can be gauged by a number of time-honored methods. For example, a quantitative measure of the order is obtained by computing the width of the lowest-order peak in the Fourier transform of the surface. A second widely employed method begins with an examination of how the surface's autocorrelation function decays with distance. If it decays exponentially, the characteristic length scale of the decay (the correlation length ξ) gives an estimate of the range over which the order extends. These methods of gauging order can be of limited use in analyzing disordered patterns: For example, the peaks in the Fourier transform may not be separable from the background or from each other, and a region of exponential decay in the autocorrelation function may not be present. Böttger et al. [7] computed the correlation length ξ for a series of imperfectly ordered hexagonal arrays of nanodots and showed that it remained nearly constant even as the order increased. Thus, even if ξ can be measured, it can be a less-than-ideal gauge of order.

Over the last decade, a powerful new tool of computational topology called persistent homology (PH) has been developed to characterize the topological properties of a set of points at all

* Corresponding author.
E-mail addresses: motta@math.duke.edu (F.C. Motta),
raneville@math.arizona.edu (R. Neville), shipman@math.colostate.edu
(P.D. Shipman), dan.pearson@colostate.edu (D.A. Pearson),
mark.bradley@colostate.edu (R.M. Bradley).

length scales [8]. It has quickly become apparent that PH is useful in a wide range of applications. In physics, it has already been employed to characterize the structure of granular media and the force networks in them [9–11], to study fluid flow [12], to probe the hierarchical structure in glasses [13], and to gauge the order of patterns produced by a model for ion bombardment of binary solids [14]. PH gives information that traditional methods do not, and has become a valuable complement to them.

The output of PH, commonly referred to as a persistence diagram or a barcode, is a multiset of (possibly repeated) ordered pairs called persistence pairs. In a study of the effect of prepatterning a binary material prior to erosion by a broad ion beam, we introduced a new quantitative measure of hexagonal order based on a scalar-valued function of these diagrams [14]. This method can be applied no matter whether the pattern produced by ion bombardment is very disordered or nearly defect free.

In this paper, we contrast several methods of quantifying the order in nearly hexagonal lattices. Section 2 motivates and defines three measures, two of which are introduced in this paper, based on persistent homology. It also defines two measures based on the Delaunay triangulation of a set of points. In Section 2, we also apply these measures to Bravais lattices and perturbations of Bravais lattices. By empirically quantifying the sensitivity of measures of hexagonal order, we highlight the value of different measures for different degrees of disorder and expose some inherent limitations of traditional methods in nearly defect-free regimes. These observations are supported by analytical calculations of the measures of order for Bravais lattices with single-point perturbations. In Section 3, we apply the measures to patterns produced by a system of partial differential equations that model nanoscale patterns formed by the ion bombardment of a solid surface. In this way, we quantify and characterize the dependence of the order on several physically-relevant system parameters. This yields new insights into the temporal evolution of the order and refines our understanding of the role of the system parameters in establishing order in different temporal regimes.

2. Measures of order

We describe in Section 2.1 geometric-combinatorial and topological tools for measuring characteristics of sets of points in the plane. In Section 2.2, we use each of these tools to define measures for order for nearly hexagonal lattices. An example of a nearly hexagonal lattice is given in Fig. 1(a), which shows a lattice L in a square region of the plane. The set L was produced from a (perfect) hexagonal lattice by displacing two points and removing one point, thus producing three defects with different degrees of severity.

2.1. Geometric-combinatorial and topological descriptions of finite sets of points

2.1.1. Delaunay triangulation

Given a set P of points in the plane, the plane may be decomposed into a Voronoi tessellation, namely the union of Voronoi polygons V_p for $p \in P$. The Voronoi polygon V_p is the set of all points in the plane that are closer to p than to any other point in P. That is, $V_p = \{x \in \mathbb{R}^2 \mid |x - p| < |x - q| \text{ for all } q \in P \text{ such that } q \neq p\}$.

The Delaunay triangulation of the set P is the graph that is dual to the Voronoi tessellation. It is constructed in the following way: The vertices of the Delaunay triangulation are the points in P, and there is an edge connecting points p and q in P if the Voronoi polygons V_p and V_q share an edge. For the lattice L shown in Fig. 1(a), the Delaunay triangulation and the Voronoi tessellation are shown in Fig. 1(b).

2.1.2. Persistent Homology

In this section, we review a novel tool of computational topology called Persistent Homology (PH) that we will use to define a topological measure of order. PH is usually employed as a means of extracting and summarizing coarse geometric features such as the number of connected components or the number of holes in high-dimensional data [8]. For us, it provides a method to both characterize the severity of individual defects in nearly hexagonal, planar lattices as well as quantify the overall degree of order with a single number. For clarity and to maintain focus on our present application, we will not formally state the algebraic and topological definitions and theorems prerequisite to our use of this tool. Our exposition is made more illuminating by carrying out the mathematical construction in the context of lattices with defects. For a complete treatment of the theory of persistent homology, consult a text on computational topology [15].

We now augment the imperfect lattice L of Fig. 1, also shown in Fig. 2(a), to construct a sequence of geometric objects, called **simplicial complexes**, consisting of vertices (the points in L), edges (pairs of points), and faces (triples of points). We denote a simplicial complex by $\mathcal{C}(L, r)$, where $r \in [0, \infty)$ is the **connectivity parameter**, such that whenever two points $a, b \in L$ are within a distance r from one another, the edge $\{a, b\}$ is included in $\mathcal{C}(L, r)$. In particular, we include the edge $\{a, b\}$ if

$$d(a, b) \leq r,$$

where $d : \mathbb{R}^2 \times \mathbb{R}^2 \to \mathbb{R}$ is the standard Euclidean metric. Also, we include the face $\{a, b, c\}$ for the connectivity parameter r if each of its three bounding edges are included, i.e., if $\max\{d(a, b), d(a, c), d(b, c)\} \leq r$.

Starting with $r = 0$, we continuously increase the connectivity parameter, building a one-parameter family of simplicial complexes. One imagines expanding disks centered at each lattice point in such a way that when the disk centered at point a intersects point b, the edge $\{a, b\}$ is added to the growing simplicial complex. In addition, when a triangle of edges is formed, the corresponding face is added to the complex. Fig. 2(b)–(d) shows examples of $\mathcal{C}(L, r)$ as r is continuously increased from $r = 0$ to $r = r_3$. Note the emergence of holes at each of the three defects for $r = r_2$ [Fig. 2(c)].

A few ideas present themselves at this point. First, the simplicial complexes constructed in this way are nested in the sense that

$$\mathcal{C}(L, r_1) \subseteq \mathcal{C}(L, r_2)$$

if $r_1 \leq r_2$. Also, there are finitely many connectivity parameters at which the simplicial complex changes (edges or triangular faces are added), and thus the nested sequence of simplicial complexes necessarily terminates, in particular at $r = \max\{d(a, b) | a, b \in L\}$. Lastly, and most importantly for us, for each geometric feature present in some simplicial complex in this one-parameter family, there exists an interval of connectivity parameters whose associated simplicial complexes contain that feature. For example, three holes (which are each topologically equivalent to circles) appear at $r = r_2$ [Fig. 2(c)]. The smallest hole, which is the least severe defect, is filled in when $r = r_3$ [Fig. 2(d)], while the two more severe defects persist and will continue to persist until larger values of r are reached.

PH, at its core, is a mathematical tool for computing the intervals of connectivity parameters over which topological features, such as connected components and holes, persist. To display and interpret the collections of intervals derived from the persistence calculation outlined above, usually one of two equivalent plots are made: a so-called **barcode**, in which intervals are stacked vertically above an axis representing the connectivity parameter, or a **persistence diagram**, in which intervals are plotted as a multiset of points in the first quadrant of $\mathbb{R}^2$, where the horizontal and vertical coordinates of a point respectively encode the starting
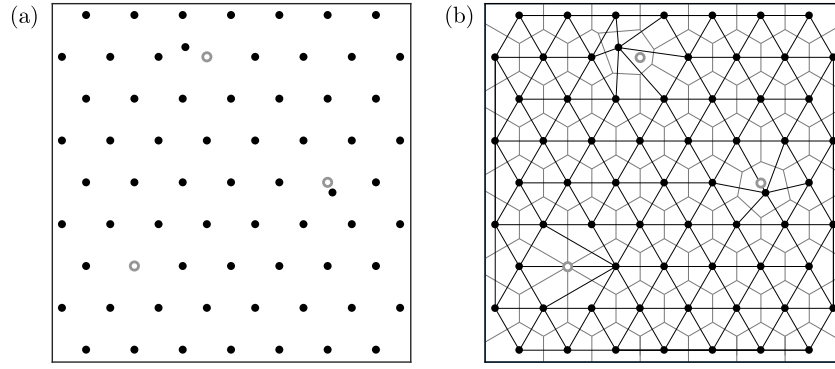
Fig. 1. (a) A nearly hexagonal lattice formed by introducing three defects into a hexagonal lattice, namely two perturbations of points and the removal of one point. (b) The Delaunay triangulation (solid lines) and Voronoi tessellation (dotted lines) of the nearly hexagonal lattice shown in (a).
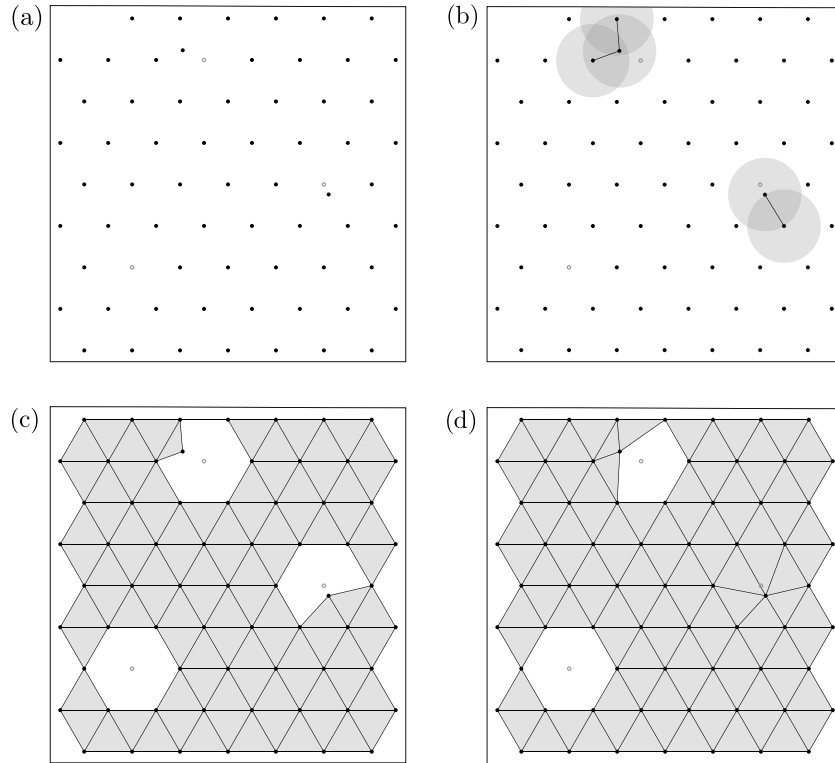
Fig. 2. Simplicial complexes with connectivity parameters (a) $r = 0$, (b) $r = r_1$, (c) $r = r_2$, (d) $r = r_3$ built on a nearly hexagonal lattice with three defects of differing severity. Here $0 < r_1 < r_2 < r_3$. Empty gray dots show the positions of the lattice points that would be present in a perfect hexagonal lattice that have been displaced or removed in the imperfectly ordered lattice. The gray disks in (b) have radius equal to the connectivity parameter r_1 which is chosen so that only a few points near defects are connected.

and ending values of the interval of r values over which a feature persists. Necessarily all points in a persistence diagram lie above the diagonal, and the vertical distance from a point to the diagonal is the length of the persistence interval.

Although both barcodes and persistence diagrams encode the same information, the former has the advantage of visually representing many intervals which have the same starting and ending values, while the latter is better suited for plotting large numbers of persistence intervals. We will use one or the other depending on which is most illuminating.

It is desirable to construct one persistence diagram for each type of topological feature. Thus, the intervals of r in which connected components persist – referred to as H_0 **intervals** in the case of a barcode, or H_0 **pairs** in the case of a diagram – are summarized in an H_0 **barcode/diagram**. Likewise, the intervals over which topological holes persist are referred to as H_1 **intervals/pairs**. Analogous

plots exist for higher dimensional features (voids, etc.) but, since our data is planar, we will concern ourselves only with H_0 and H_1 diagrams.

Fig. 3 shows the H_0 and H_1 barcodes and persistence diagrams for our example of a nearly hexagonal lattice. Notice the variance in the lengths of the intervals in the H_0 barcode. All connected components collapse into a single connected component at the connectivity parameter $r = r_2$, the nearest-neighbor distance in the hexagonal lattice without defects. However, the three defects result in the termination of some bars at values of r less than r_2. Notice that an infinitely long bar will be found in every H_0 barcode since exactly one connected component persists for all $r \in [0, \infty)$ for any finite set of points.

In the H_1 persistence diagram [Fig. 3(d)] there are three distinct points representing the three intervals of persistence for the three topological circles (holes) corresponding to the three defects. Note
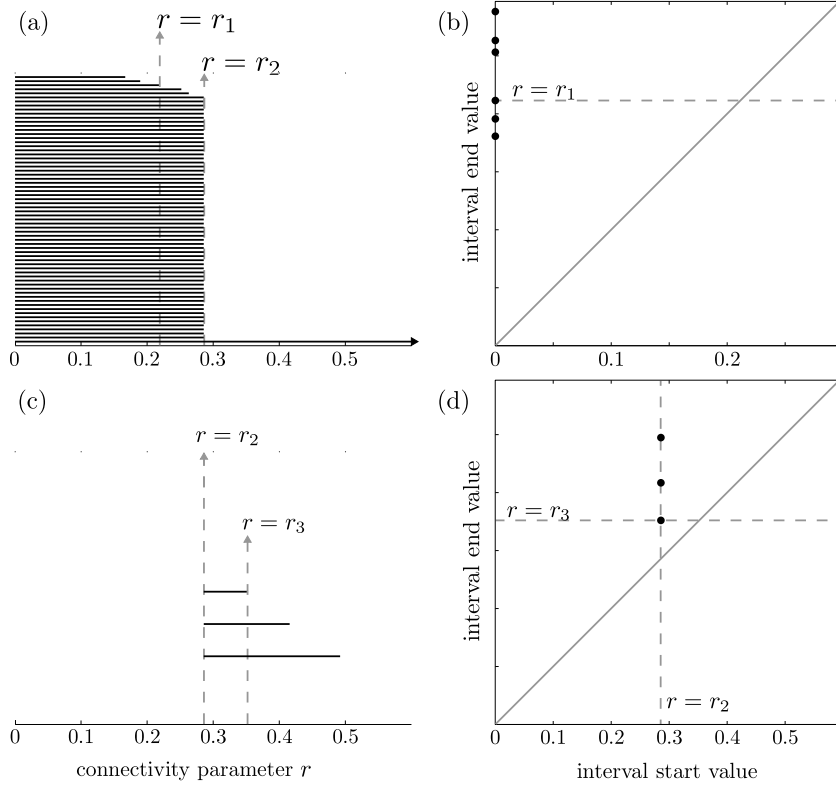
Fig. 3. The H_0 (a) barcode, and (b) persistence diagram, as well as the H_1 (c) barcode and (d) persistence diagram for the nearly hexagonal lattice shown in Fig. 2. The connectivity parameters for the panels of Fig. 2 are highlighted with dashed lines.

the differences in the vertical distances between each point and the diagonal: the more severe the defect, the larger this distance. Fig. 3(c) shows the corresponding barcode where the persistence intervals in r are explicitly drawn. Each of the three holes appear precisely at $r = r_2$ because the underlying set of points in this example is nearly perfectly hexagonal.

The details of the persistence homology algorithm are beyond the scope of this paper, but can be found in [15]. Presently there are a number of well-maintained open-source packages, developed to interface with various suites of scientific computing software, which efficiently compute the persistent homology of a point cloud [16–19].

2.2. Characterizations of hexagonal order

Having introduced the Delaunay triangulation and persistent homology, we are prepared to define and compare several measures of the order in nearly hexagonal lattices. We motivate and define these measures through the consideration of Bravais lattices in Section 2.2.1. An ideal measure of hexagonal order should designate only a perfectly hexagonal Bravais lattice to be perfectly ordered. We then test the measures on perturbed Bravais lattices in Sections 2.2.2 and 2.2.3.

2.2.1. Bravais lattices

A Bravais lattice in $\mathbb{R}^2$ is the integer linear combination

$$\mathbb{L}(\boldsymbol{v}_1, \boldsymbol{v}_2) = \{z_1 \boldsymbol{v}_1 + z_2 \boldsymbol{v}_2 \mid z_i \in \mathbb{Z}\}$$

of a basis $\{\boldsymbol{v}_1, \boldsymbol{v}_2\}$ for $\mathbb{R}^2$. Two Bravais lattices $\mathbb{L}_1$ and $\mathbb{L}_2$ are equivalent for our purposes if there exists an angle-preserving linear transformation (a combination of a dilation, a rotation, and a reflection) that is a bijection between them. The shaded regions in Fig. 4 depict two representations of the entire set of equivalence classes of Bravais lattices that are determined as follows: Given a

Bravais lattice $\mathbb{L}$, choose a shortest vector $\boldsymbol{u}' \in \mathbb{L}$ and a vector $\boldsymbol{v}' \in \mathbb{L}$ that is a vector of minimal length not in the span of $\boldsymbol{u}'$. For any such vector $\boldsymbol{v}'$, $-\boldsymbol{v}'$ also satisfies the same condition. This allows us to choose $\boldsymbol{v}'$ so that $|\boldsymbol{u}' - \boldsymbol{v}'| \leq |\boldsymbol{u}' + \boldsymbol{v}'|$, or equivalently so that the angle θ between $\boldsymbol{u}'$ and $\boldsymbol{v}'$ satisfies $0 < \theta \leq \frac{\pi}{2}$. These choices imply that $|\boldsymbol{u}'| \leq |\boldsymbol{v}'| \leq |\boldsymbol{u}' - \boldsymbol{v}'|$. Now let T be the angle-preserving linear transformation of $\mathbb{R}^2$ such that $T(\boldsymbol{u}' - \boldsymbol{v}') = (1, 0)$ and $T(\boldsymbol{u}')$ lies in the first quadrant. T is a combination of a dilation (by $1/|\boldsymbol{u}' - \boldsymbol{v}'|$), a rotation, and a reflection. Write $\boldsymbol{u} = T(\boldsymbol{u}') = (x, y)$, $\boldsymbol{v} = T(\boldsymbol{v}')$, and $\boldsymbol{w} = T(\boldsymbol{u}' - \boldsymbol{v}') = \boldsymbol{u} - \boldsymbol{v} = (1, 0)$. The choices of $\boldsymbol{u}'$, $\boldsymbol{v}'$ and T imply that $x, y > 0$; $|\boldsymbol{u}| \leq |\boldsymbol{v}| \leq 1$; and $|\boldsymbol{u} - \boldsymbol{v}| \leq |\boldsymbol{u} + \boldsymbol{v}|$. These constraints determine a region R in $\mathbb{R}^2$ in which $\boldsymbol{u} = (x, y)$ may lie. R is the region satisfying the following constraints:

1. $|\boldsymbol{u}| \leq 1$ implies that $x^2 + y^2 \leq 1$.
2. $|\boldsymbol{v}| \leq 1$ implies that $(x - 1)^2 + y^2 \leq 1$.
3. $|\boldsymbol{u}| \leq |\boldsymbol{v}|$ implies that $x \leq \frac{1}{2}$.
4. $|\boldsymbol{u} - \boldsymbol{v}| \leq |\boldsymbol{u} + \boldsymbol{v}|$ (equivalently, $0 \leq \boldsymbol{u} \cdot \boldsymbol{v}$) implies that $x^2 - x + y^2 \geq 0$.

The upper left panel of Fig. 4 depicts the shaded region R in the x–y plane. A choice of $\boldsymbol{u} = (x, y)$ outside of this region determines a lattice that may be transformed to one in R by an angle-preserving linear transformation. The colors code for curves on which $\boldsymbol{u} \cdot \boldsymbol{v} = 0$ (green), $|\boldsymbol{u}| = |\boldsymbol{v}|$ or $|\boldsymbol{u}| = |\boldsymbol{w}|$ (red), and $|\boldsymbol{v}| = |\boldsymbol{w}|$ (blue).

Examples of Bravais lattices and the fundamental triangle Δ formed by the vector triad $\boldsymbol{u}$ (colored, dotted), $\boldsymbol{v}$ (black, dotted), and $\boldsymbol{w}$ (black, solid line) are shown in the second row of Fig. 4. The side lengths of the fundamental triangle Δ are $L_1 \equiv |\boldsymbol{u}|$, $L_2 \equiv |\boldsymbol{v}|$, and $|\boldsymbol{w}| = 1$, as depicted in the upper central panel of Fig. 4. It is helpful to also visualize the region R in terms of the side lengths L_1 and L_2 of Δ, as depicted in the upper right panel of Fig. 4.

For each example Bravais lattice in Fig. 4, the position of the corresponding fundamental triangle is marked in the plots of the
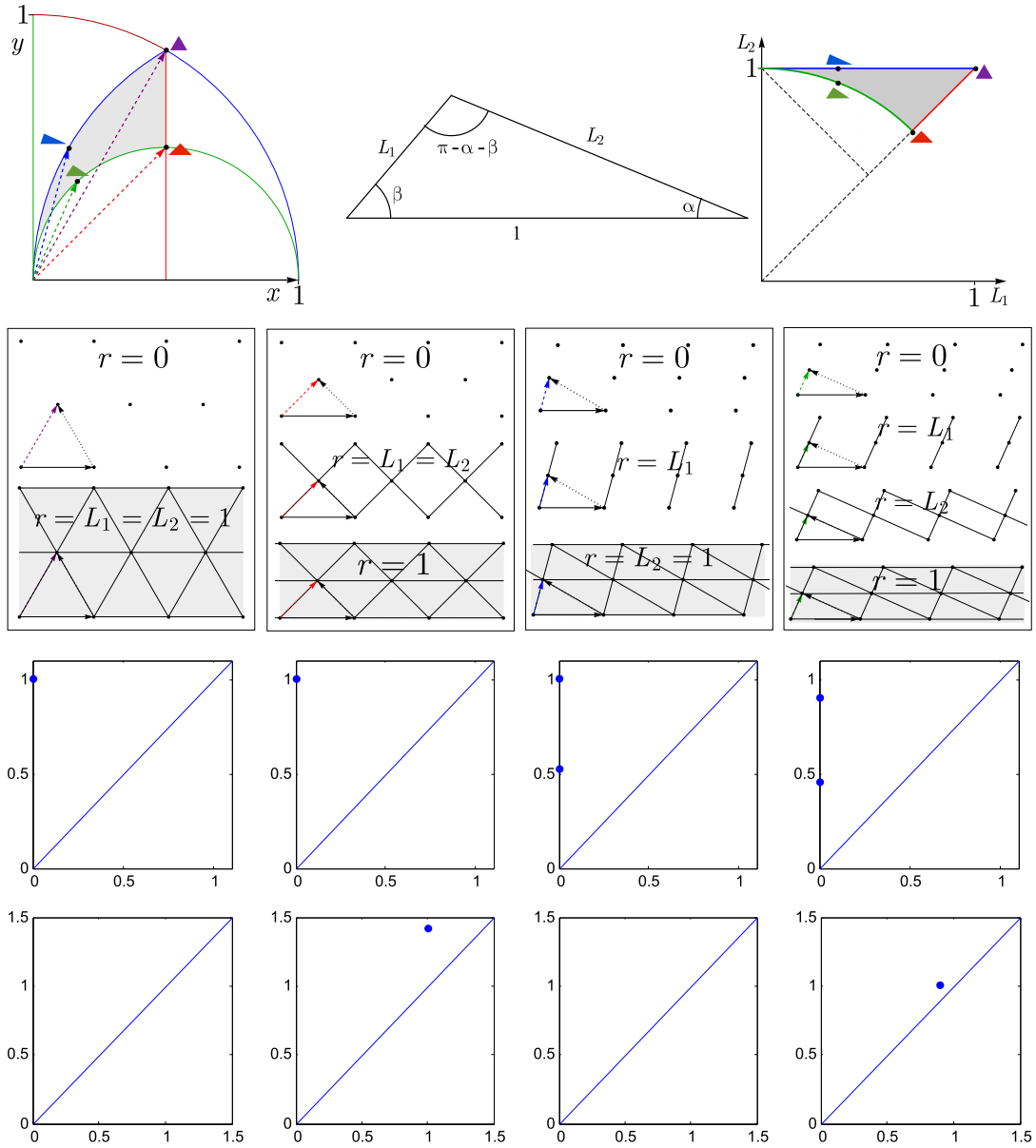
Fig. 4. Top row: The region R (shaded) parameterizing the space of inequivalent Bravais lattices in the x–y plane (first column) and the $L_1 - L_2$ plane (third column), where as depicted in the second column, the side lengths of a fundamental triangle for the Bravais lattice are $L_1 \leq L_2 \leq 1$. Second row: Each column is an example of a Bravais lattices and the sequence of simplicial complexes formed for values of the connectivity parameter r noted on the diagrams. For each sample Bravais lattice, the vector $(1, 0)$ is marked by a solid black arrow, the vector $\boldsymbol{u}$ that lies in the region R is marked by a dashed colored arrow, and the vector $\boldsymbol{v}$ (see text) is marked by a dashed black arrow. These vectors form the fundamental triangle for the lattice. For each sample lattice, the vector $\boldsymbol{u}$ and the shape of the fundamental triangle is marked on the depiction of the region R in the first column of the first row. The H_0 and H_1 persistence diagrams for the sample Bravais lattices are shown in the third and fourth rows, respectively. (For interpretation of the references to colour in this figure legend, the reader is referred to the web version of this article.)

region R. These examples include a hexagonal lattice ($L_1 = L_2 = 1$; purple), a square lattice ($L_1 = L_2 = 1/\sqrt{2} < 1$; red), a lattice for which $L_1 < L_2 = 1$ (blue), and a lattice for which $\boldsymbol{u} \cdot \boldsymbol{v} = 0$ and $L_1 < L_2 < 1$ (green).

Measures of order using the Delaunay triangulation:

We define two measures of order using the Delaunay triangulation. For a perfect hexagonal lattice, the degree of each vertex in the Delaunay triangulation is 6. For the square or rectangular Bravais lattice, the number of nearest neighbors of any point is 4. Defects in a lattice can alter the degree of vertices in the Delaunay triangulation, as shown in Fig. 1(b). The Nearest Neighbor Number (N³) measure is computed by taking the variance of $N_i - 6$, where N_i is the number of nearest neighbors of the ith lattice point. This will give a N³ score of 0 for a perfect hexagonal lattice. The N³ measure is,

however, a very crude measure of hexagonal order, since the N³ of any lattice that is not rectangular (such as a square lattice) is also 0.

The Delaunay Triangulation (DT) measure of order is a statistic on the lengths of the edges in a Delaunay triangulation, introduced by Mátéfi-Tempfli et al. [20]. For perfect hexagonal ordering, each triangle in the triangulation is equilateral. We compute the dominant edge length, L_{dom}, for a lattice by averaging over all edge lengths appearing in the triangulation. We then assign to each triangle the score $L_{i,dev} = \sum_{k=1}^{3} |L_{i,k} - L_{dom}|$, where $L_{i,k}$ is the edge length of the kth edge of the ith triangle. The DT measure is the value of $L_{i,dev}$ averaged over all triangles. For a perfect hexagonal lattice, the DT measure is 0.

In the Delaunay triangulation, triangles appearing along the edges of the domain can be highly distorted. To avoid edge effects from such triangles, we tile the area surrounding the lattice with

copies of the same lattice, compute the triangulation of the tiled domain and only retain edges that appear both in the triangulation of the original domain and the extended domain.

For a Bravais lattice, the DT measure of order in terms of the side lengths of the fundamental triangle Δ is $\frac{2}{3}(1 - 2L_1 + L_2)$ if $L_2 > \frac{1}{3}(L_1 + L_2 + 1)$ and $\frac{2}{3}(2 - L_1 - L_2)$ if $L_2 < \frac{1}{3}(L_1 + L_2 + 1)$. We show in the first and third panels of Fig. 5 the DT measure of order as a function of Bravais lattice in the region R. Note that the DT measure is the same for all lattices with $L_1 = L_2$ (marked by the red curves in the figures).

The PH measures of order:

The first step in using PH to measure hexagonal order in Bravais lattices is to determine the nested sequence of simplicial complexes formed as the connectivity parameter r increases. For the four example Bravais lattices of Fig. 4, we show the entire nested sequence of simplicial complexes (second row), and the corresponding H_0 (third row) and H_1 (fourth row) persistence diagrams. For all lattices represented by points in the interior of the region R as well as those on the green curve given by $\boldsymbol{u} \cdot \boldsymbol{v} = 0$, we have that $0 \leq L_1 \leq L_2 \leq 1$. For these lattices, there are four simplicial complexes in the nested sequence, as illustrated by the fourth column of Fig. 4.

Bravais lattices are infinite sets, and their persistence diagrams have either 0 or an infinite number of bars. The intersection of a Bravais lattice with a bounded simply connected subset Ω of the plane (a *finite Bravais lattice*) has persistence diagrams with finite numbers of bars. The shape of Ω affects the persistence diagram.

Recall that the H_0 persistence diagram is computed from the changes in the numbers of components in the simplicial complex as r increases. The number of components of a finite Bravais lattice is equal to the number of points at $r = 0$, decreases at $r = L_1$, and decreases to 1 at $r = L_2$. For the hexagonal lattice, $L_1 = L_2$, and so there is only one bar length. The variance of the barlengths in the H_0 persistence diagram is therefore 0 for the infinite perfect hexagonal lattice.

As our first topological measure of order, we define $\text{var}(H_0)$ to be the variance of the lengths of the bars in the H_0 persistence diagram. For a Bravais lattice, the contribution of each fundamental triangle to the H_0 variance is

$$\text{var}(H_0)_\Delta = \frac{1}{4}(L_2 - L_1)^2.$$

The H_1 persistence diagram is computed by observing changes in the numbers of topological holes in the simplicial complex as r increases. For a Bravais lattice, topological holes form at $r = L_2$ and are filled in by faces at $r = 1$. Since $L_2 = 1$ for a perfect hexagonal lattice, the H_1 persistence diagram for such a lattice is empty (devoid of bars). We define a second topological measure of order as the sum of all the lengths of the bars in the H_1 persistence diagram and call this the H_1 sum, ΣH_1. For a Bravais lattice, the contribution of each fundamental triangle to the H_1 sum is therefore

$$\Sigma H_{1,\Delta} = 1 - L_2.$$

The PH of a point cloud carries geometric information and depends on the overall scale of the cloud. In particular, a rescaling of a set of points in $\mathbb{R}^2$ by a constant factor will correspondingly scale the starting and ending values of each interval over which a topological feature persists by that same factor, and thus ΣH_1 will be likewise scaled. Moreover, ΣH_1 may depend on the density of points in a fixed domain. For example, consider the finite subset of the square lattice $S_n \equiv \{(i, j)/n \mid 0 \leq i, j \leq n-1\} \subset \mathbb{L}(\boldsymbol{e}_1/n, \boldsymbol{e}_2/n)$, where $\boldsymbol{e}_1 \equiv (1, 0)$ and $\boldsymbol{e}_2 \equiv (0, 1)$. Then

$$\Sigma H_1(S_n) = (\sqrt{2} - 1)\left(n - 2 + \frac{1}{n}\right),$$

showing that $\Sigma H_1(S_n)$ scales with the square-root of the point density for large n. Thus, PH measures of order should only be compared between planar arrangements with the same number of points that have been normalized to the same domain.

Fig. 6 shows $\text{var}(H_0)_\Delta$ (first column) and $\Sigma H_{1,\Delta}$ (second column) as functions of position in the region R; darker shading indicates a larger value. Along the line $L_1 = L_2$, which includes both the hexagonal and square lattices, $\text{var}(H_0)_\Delta$ is identically 0. For $L_2 = 1$, $\text{var}(H_0)_\Delta$ increases with decreasing L_1, approaching a maximum value of $\frac{1}{4}$ as L_1 approaches 0. On the other hand, $\Sigma H_{1,\Delta}$ ranges from 0 (along the segment $L_2 = 1$) to $(\sqrt{2} - 1)/\sqrt{2}$ (at $L_1 = L_2 = 1/\sqrt{2}$).

The values $\text{var}(H_0)_\Delta$ and $\Sigma H_{1,\Delta}$ are equal to zero along different 1-dimensional curves that intersect at exactly one point, namely the point representing the hexagonal lattice. Hence, although neither measure completely distinguishes the hexagonal lattice from other Bravais lattices, a linear combination $c_1 \text{var}(H_0)_\Delta + c_2 \Sigma H_{1,\Delta}$ with positive constants c_1 and c_2 is equal to zero only for the hexagonal lattice. Choosing $c_1 = 2$ and $c_2 = 1/(2 - \sqrt{2})$ so that the maximum values of $c_1 \text{var}(H_0)_\Delta$ and $c_2 \Sigma H_{1,\Delta}$ in the region R are both equal to $\frac{1}{2}$, we plot in the third column of Fig. 6 the combined PH measure of order

$$CPH_\Delta = \frac{1}{2}(L_2 - L_1)^2 + \frac{1}{2 - \sqrt{2}}(1 - L_2)$$

for a Bravais lattice. More generally, we define the combined PH measure of order to be

$$CPH = 2\text{var}(H_0) + \frac{1}{2 - \sqrt{2}}\Sigma H_1.$$

Having defined several measures of order for the entire class of unperturbed Bravais lattices, we now compare these quantities by studying how they gauge disorder by introducing defects to a hexagonal Bravais lattice.

### 2.2.2. Bravais lattices perturbed at one point

To understand the sensitivity of each measure to small perturbations in the lattice, we start by perturbing a single point in a perfect hexagonal lattice. In Fig. 7, we show the various measures of order as functions of the position of the perturbed point. The point at the center of the hexagon represents a perfect, unperturbed lattice. The vertices of the hexagonal region are the nearest unperturbed lattice points. From this, we can see a large region in which the N^3 measure is invariant to a perturbation of the center point. In fact, in the entire central region, the value of the N^3 measure is zero since the center is not perturbed enough to change the configuration of the Delaunay triangulation. For the same reason, the DT measure displays a small discontinuity at the boundary of the region where the N^3 equals zero. Notably, the measure ΣH_1 appears to be most sensitive to perturbations of the lattice point when that point is near to the center, i.e. when the lattice is very close to perfectly hexagonal. On the other hand, $\text{var}(H_0)$ is insensitive to changes in the position of the central lattice point when that point is near the center of the hexagon and apparently more sensitive in a region bounded away from the center of the hexagon.

### 2.2.3. Randomly perturbed Bravais lattices

To test the sensitivity of each measure to noise in a lattice, we compute each for lattices produced by randomly perturbing every point of a perfectly hexagonal lattice. We start with a perfect hexagonal lattice comprised of 2500 points. Each point is displaced from its original position in a random direction (chosen from a uniform distribution) by a distance $\mu\delta$, where μ is a fixed scaling factor and δ is chosen from a uniform distribution. The mean and variance of the measures of order over 100 trials at each value of
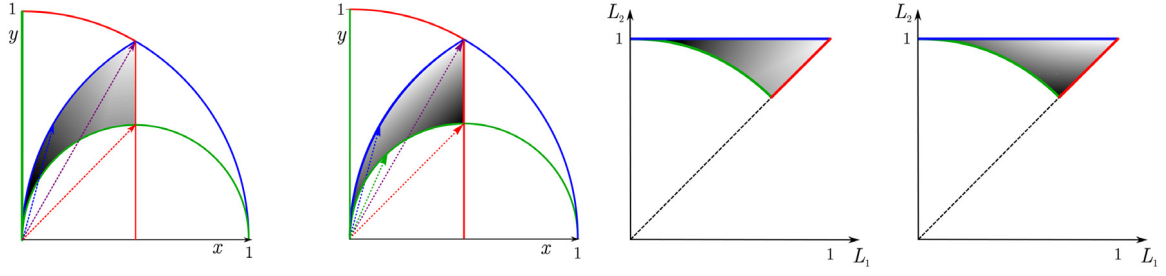
Fig. 5. Gray-scale plots (with darker shading indicating larger values) of the DT (panels 1 and 3) and total PH (panels 2 and 4) measures of order within the region R parameterizing Bravais lattices, depicted in the x–y plane (panels 1 and 2) and the $L_1 - L_2$ plane (panels 3 and 4).
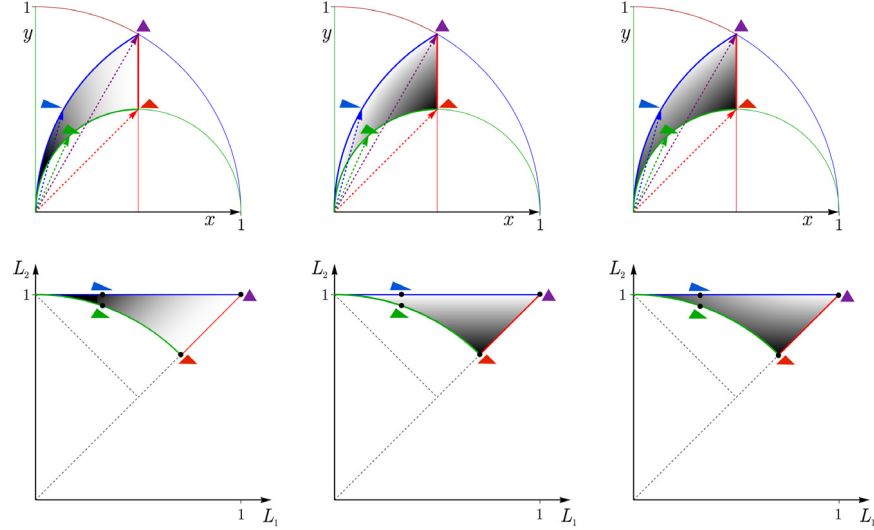
Fig. 6. Gray-scale plots (with darker shading indicating larger values) of the PH measures of order within the region R parameterizing Bravais lattices, depicted in the x–y plane (top row) and the $L_1 - L_2$ plane (bottom row). The measures $\mathrm{var}(H_0)_\Delta$, $\Sigma H_{1,\Delta}$, and CPH_Δ are respectively graphed in the first, second, and third columns.
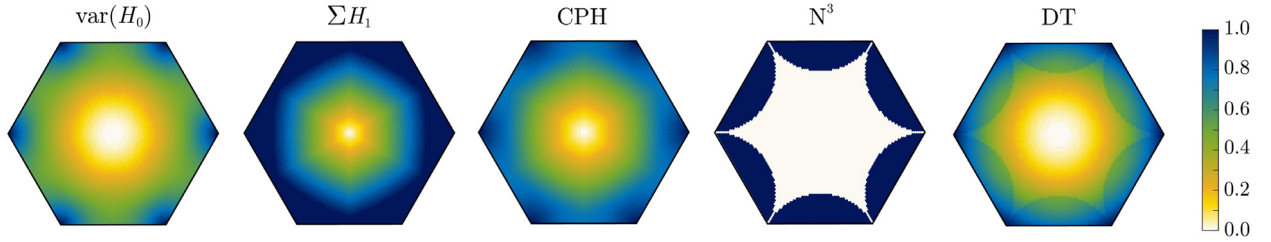
Fig. 7. Measures of order for a perfect hexagonal lattice with the center point perturbed: (left to right) $\mathrm{var}(H_0)$, ΣH_1, CPH, N^3, and DT. The location of the plotted point gives the location of the perturbed center point and the color indicates the value of the measure for each configuration. Each measure has been normalized based on the values of the measure in this region.

the scaling factor μ ranging from 0.01 to 1 are shown in Fig. 8 as a function of μ.

To allow for a fair comparison of the various measures, each measure was normalized so that its mean value would be 1 for a set of points chosen randomly with a uniform distribution. The value of the normalization was found by computing each measure of order for 500 trials of 2500 points drawn from a uniform distribution on the same square domain used for the randomly perturbed Bravais lattices.

The N^3 measure is insensitive to low levels of noise. In fact, N^3 will not detect any perturbations at sufficiently small noise levels since the neighbors of a perturbed hexagonal lattice (as determined by the Delaunay triangulation) will not change until the perturbations are sufficiently large. On the other hand, in this noise regime, ΣH_1 is highly sensitive. As the noise increases, ΣH_1 reaches a maximum value and then slightly decreases. However,

this is a regime in which $\mathrm{var}(H_0)$ appears to be most sensitive to changing noise levels. The CPH measure allows us to capitalize on the sensitivity of the $\mathrm{var}(H_0)$ and ΣH_1 measures in different regimes. The DT measure displays a similar degree of sensitivity to μ. All of these observations are consistent with the sensitivity of each measure to a single point perturbation in an otherwise perfect hexagonal lattice [see Fig. 7].

3. Application to patterns produced by ion bombardment of solid surfaces

A variety of experiments have shown spontaneous nanoscale pattern formation on a solid surface can result from broad ion beam erosion [21–25]. Among these is the striking observation that normal-incidence ion bombardment of the binary compound GaSb can produce nearly regular hexagonal arrays of nanodots [3].
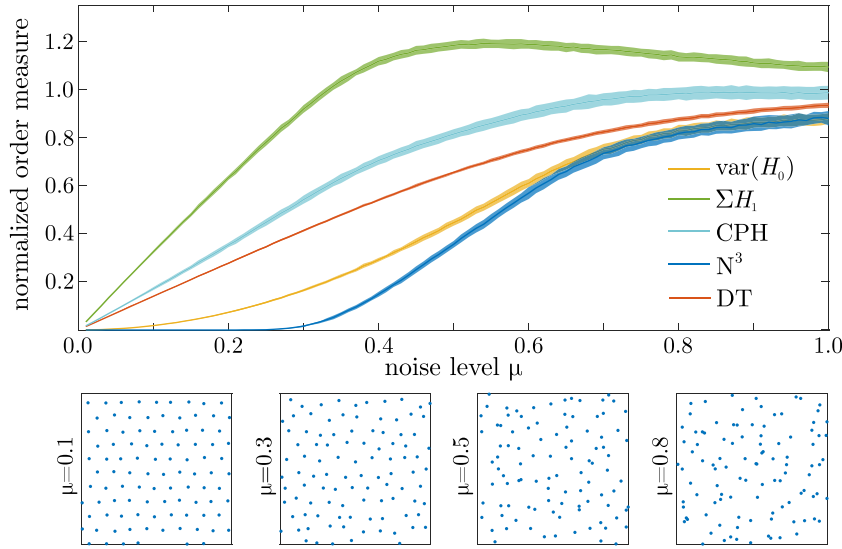
Fig. 8. Top panel: Plot of the normalized measures for perturbed lattices as functions of noise level μ. The error bars indicate the variance of the measures over 100 trials. Each measure has been normalized so that its expected measure has a value of one for points drawn from a uniform distribution. Bottom panels: Examples of a section of the lattice for increasing degrees of noise.

An important piece of the analysis of experimental surface data is quantifying global hexagonal order, both for comparisons for a variety of experimental conditions (*e.g.*, ion beam energy, target material, angle of ion incidence, etc.) and for model validation.

In this section we apply the measures of hexagonal order defined in Section 2.1 as well as a commonly employed spectral method to simulations of surfaces undergoing erosion by a broad ion beam at normal incidence. This section serves to compare the measures of hexagonal order described in this paper in the context of a particular model of spontaneous nanoscale pattern formation, make novel observations regarding the dynamics of this system, and motivate the application of our techniques to experimentally derived surface data.

We now introduce a common spectral method which will be compared to the measures of order on lattices. Periodicity is reflected in the magnitude of the Fourier spectrum. If the surface is a perfect (periodic) hexagonal arrays of nanodots, the spectrum is concentrated most prominently at the six fundamental wave vectors (oriented 60 degrees apart) associated with the hexagonal pattern. Deviations from perfect periodicity, for example the presence of multiple orientations of hexagonal arrays or other defects, cause the active Fourier modes to spread into an annular region. To measure this spread, we first compute the radial average of the power spectral density. Next, we measure full width at half maximum (FWHM) of the highest Fourier peak in the radial average. A narrow peak indicates a nearly perfect lattice or a high degree of hexagonal order, while a wider peak indicates that there are significant deviations from a perfect hexagonal pattern.

Shenoy, Chan and Chason first studied the coupling between the surface topography and composition that arises during ion bombardment of a binary compound [26]. Bradley and Shipman (BS) extended this theory to include the effect of mass redistribution and the leading order nonlinear terms [4–6]. The BS equations govern the behavior of the deviations of the surface height, $u(x, y, t)$, and surface concentration of one of the two atomic species, $\phi(x, y, t)$, from their unperturbed, steady-state values. Using the same notation, assumptions and rescaling as BS employed, we have

$$\frac{\partial u}{\partial t} = \phi - \nabla^2 u - \nabla^2 \nabla^2 u + \lambda (\nabla u)^2,$$
$$\frac{\partial \phi}{\partial t} = -a\phi + b\nabla^2 u + c\nabla^2 \phi + \nu \phi^2 + \eta \phi^3 \qquad (1)$$

for normal-incidence bombardment. Explicit expressions that relate the dimensionless constants a, b, c, λ, ν and η to the underlying physical parameters may be found in Ref. [6].

Linear stability analysis of the system given by (1) reveals that in the parameter region S in which $c > a$ and $4a > (1 - c)^2$ if $c < 1$, the spatially uniform solution with $u = 0$ and $\phi = 0$ is stable for values of b above a critical value $b_T \equiv (a + c)^2/(4c)$ [4,6]. For values of b smaller than b_T, the state $u = \phi = 0$ is unstable to perturbations of the form

$$\begin{pmatrix} u \\ \phi \end{pmatrix} = \begin{pmatrix} u_* \\ \phi_* \end{pmatrix} \exp(i\boldsymbol{k} \cdot \boldsymbol{x} + \sigma(k)t), \qquad (2)$$

where u_* and ϕ_* are constants, $\boldsymbol{k} \equiv k_x \hat{x} + k_y \hat{y}$, $\boldsymbol{x} \equiv x\hat{x} + y\hat{y}$, and $k \equiv |\boldsymbol{k}|$. Re $(\sigma(k))$ gives the rate with which the amplitude of the Fourier mode (2) grows or attenuates. In the parameter region S, if b is slightly less than b_T, then Re $(\sigma(k)) > 0$ in a narrow band of wave numbers centered on a critical wave number

$$k_T \equiv \sqrt{(c - a)/2c}.$$

If $b_T - b$ is small, a well-ordered hexagonal array of nanodots forms. As $b < b_T$ is decreased, $\sigma(k_T)$ and, correspondingly, the width of the annulus of linearly unstable wave numbers grows. Therefore, it is reasonable to expect that hexagonal order will diminish as b is decreased and the band of active modes broadens. Furthermore, it has been hypothesized that defects are more likely to persist for values of the parameters that lead to an increased growth rate of the amplitude of the neutrally-stable wave vector $\boldsymbol{k} = \boldsymbol{0}$ (the so-called zero, soft, or Goldstone mode), which interacts with finite wavelength unstable modes through the nonlinearities in the system (1) [27]. Thus, to characterize the time evolution of global hexagonal order and explore parametric control of defect formation and elimination, we apply the measures defined in Section 2.1 and the spectral method to numerical simulations of the system (1) for different choices of bifurcation parameter b and for parameter choices that give different growth rates of the amplitude of the zero mode.

In [6], the authors observed that the maxima in the field $1 - \phi$ were nearly coincident with the maxima of u. We therefore do not expect there to be significant differences between the measures of hexagonal order in the composition field ϕ and surface topography u, although the methods outlined in Section 2 apply equally well

to both. Accordingly, we will restrict our analysis to the hexagonal order in u.

For each choice of system parameters, 50 simulations were initialized with low-amplitude white noise on a 256×256 grid. Identical initial conditions were used for each choice of parameters. Numerical integration of Eq. (1) was conducted using a Fourier spectral method with periodic boundary conditions and a fourth-order exponential time differencing Runge–Kutta method for the time stepping [28,29]. For each simulation, we retained a time series of 100 surfaces. For each surface, the locations of the nanodot maxima were determined using finite differences. Thus, each simulation was transformed into a time series of 100 planar point clouds representing the maxima of the surface nanodots.

Some care is needed to eliminate spurious boundary effects that would otherwise introduce bias into some of our measures of hexagonal order. In particular, nanodot neighbors should be determined in a manner which respects the periodic boundary conditions used in the simulations. Thus, to properly represent the nanodot point cloud as belonging to a torus without boundary, we first tiled the plane with 9 vertically and/or horizontally translated copies of each surface to form a 3×3 grid, aligned in accordance with the periodic boundary conditions. Hexagonal order statistics were then computed for the original set of nanodots in the central copy of the surface in 3×3 grid, while also accounting for nanodot neighbors that belong to the other, translated copies of the surface. For example, to calculate the average number of the neighbors of each nanodot, a Voronoi tessellation was constructed on the planar point cloud of local maxima of the tiled surface, while the number of neighbors was determined only for those nandots in the original surface domain. Similarly, neighbor edge lengths in the Delaunay triangulation were taken to be the distance between nanodot neighbors, accounting for the periodic boundary conditions.

Note that the most linearly unstable wave number, k_T, does not depend on the bifurcation parameter, b. However, as a surface evolves away from the unstable flat steady state, nonlinear effects influence the characteristic wavelength of the observed pattern, and therefore the average spacing between neighboring nanodots. For instance, we find that – after a long erosion time (simulation time $t = 60{,}000$) – the average number of nanodots in a square domain with fixed dimensions decreases by roughly 5% when b is increased from $0.90b_T$ to $0.99b_T$. This is a concern since, as discussed in Section 2.1.2, unnormalized ΣH_1 values may reflect both global order and point cloud density. Therefore, we fix the number of points in each point cloud by retaining a fixed, chosen number of points in each point cloud with the smallest L_∞ norm. We then scale the retained subset of the point cloud to the region $[-1, 1] \times [-1, 1]$. In an experimental setup, this would amount to choosing a square subregion of a patterned surface containing a predetermined number of nanodots, and then dilating the region to fit in the square $[-1, 1] \times [-1, 1]$.

Normalization ensures that the PH statistics are not biased by domain size or the number of nanodots within the domain. This is an essential step to tracking topological order statistics over time and for comparison of simulated and experimental data. Indeed, the size of an experimental sample domain and the number of nanodots contained therein depend on the chosen experimental conditions. That said, it is always possible to fix the nanodot density by first restricting the domain to a region containing a specified number of dots, and then rescaling the domain dimensions.

3.1. Dependence of order on the bifurcation parameter

To test the hypothesis that hexagonal order diminishes as the bifurcation parameter is reduced below the critical point $b = b_T$, we performed 50 simulations of the system (1) with $b = 0.99b_T$

and $0.90b_T$ with each pair of trials initiated from the same low-amplitude white noise initial condition. All other system parameters were fixed. The values $a = 0.25$, $c = 1$, $\nu = 0.75$, $\lambda = 0$, and $\eta = 10$ were chosen to belong to the regime in which the BS system is known to undergo a Turing bifurcation at $b_T = (a+c)^2/(4c)$ and its solutions exhibit hexagonal arrangements of nanodots at long times [4].

By simulation time $t = 60{,}000$ (the maximum time to which simulations were carried out), each of the measures ΣH_1, CPH, N^3, DT, and FWHM suggest with high confidence that the expected hexagonal order is improved for the choice of the bifurcation parameter, b, nearer to b_T (see Table 1). However, plots of the order statistics ΣH_1, var(H_0), CPH, N^3, and DT, versus time [Fig. 9] reveal that the hexagonal order during the initial, transient dynamics is much better for $b = 0.90b_T$ than for $b = 0.99b_T$.

One possible explanation for the counter-intuitive behavior of the early-time order is that since Re $(\sigma(k_T))$ increases as b is decreased, moving away from criticality forces a rapid commitment to a poorly ordered surface in the linear regime. Later this slows the rearrangement of well-ordered patches into a consistently oriented global hexagonal lattice. This hypothesis is supported by visual inspection of the surfaces and the corresponding H_1 persistence diagrams, as shown for snapshots of representative simulations in Fig. 10. Notice that by time $t = 6000$, nanodots are already well formed for $b = 0.90b_T$. Moreover, the number of topological holes and their persistence intervals are significantly smaller for $b = 0.90b_T$ than $b = 0.99b_T$ at this early time. On the contrary, by time $t = 60{,}000$, the overall hexagonal order in the surface evolving with $b = 0.90b_T$ has improved very little as compared to surfaces evolving with $b = 0.99b_T$, whose persistence diagrams show a reduction in the overall number and persistence of defects.

Interestingly, the FWHM does not capture the observation that rapid commitment to a pattern may hinder long-term order, as the FWHM curves in Fig. 9 are nearly identical for the two different parameter choices over short time scales and only convincingly separate at later times. Note that improved overall hexagonal order is reflected in an increase in the amplitudes of modes at a characteristic wavelength oriented 60 degrees apart and a reduction in the amplitudes of modes with the same wavelength but with differently oriented wave vectors. Thus, since the FWHM is computed from the radially averaged power spectral density function, it is not able to distinguish between a narrow band of active modes that are well-distributed in some annulus of wave vectors and highly concentrated active modes arranged hexagonally in that annulus.

3.2. Dependence of order on the zero mode

Weakly nonlinear analysis of Eqs. (1) yields ordinary differential equations describing the growth rates of the amplitudes of Fourier modes as the system evolves away from the steady state $u = \phi \equiv 0$, including the real-valued amplitude corresponding to the neutrally-stable wave vector **0**, whose derivative is the spatially-averaged rate of recession of u [6]. In particular, we write

$$\begin{pmatrix} u \\ \phi \end{pmatrix} = \sum_{i=0}^{\infty} \epsilon^i \begin{pmatrix} u_i \\ \phi_i \end{pmatrix},$$

where $u_0 = \phi_0 \equiv 0$ is the uniform unstable steady-state solution. The first-order term is found to be

$$\begin{pmatrix} u_1 \\ \phi_1 \end{pmatrix} = \sum_{|\mathbf{k}|=k_T} \begin{pmatrix} 1 \\ \frac{a^2 - c^2}{4c^2} \end{pmatrix} (A_{\mathbf{k}} e^{i\mathbf{k} \cdot \mathbf{x}} + c.c.) + \begin{pmatrix} Z \\ 0 \end{pmatrix}.$$

Equations for the time evolution of the complex-valued amplitudes, $A_{\mathbf{k}}$, and the real-valued amplitude of the zero mode, $Z(t)$, are determined by applying a solvability condition at order ϵ^2. It is

Table 1

Distribution statistics for measures of hexagonal order at time $t = 60{,}000$ and the p-value of the two-sided Mann–Whitney–Wilcoxon (MWW) U-test that tests the null hypothesis that the order measures for two different parameter choices are equally distributed.

Measure	Mean		Std. dev.		MWW test p-value
	$0.99b_T$	$0.90b_T$	$0.99b_T$	$0.90b_T$	
ΣH_1	1.294×10^0	1.424×10^0	1.960×10^{-1}	1.992×10^{-1}	5.88×10^{-3}
$\mathrm{var}(H_0)$	3.645×10^{-3}	3.646×10^{-3}	5.382×10^{-6}	6.962×10^{-6}	8.34×10^{-1}
N^3	1.065×10^{-1}	1.323×10^{-1}	3.008×10^{-2}	2.184×10^{-2}	3.66×10^{-6}
DT	2.024×10^{-2}	2.212×10^{-2}	2.201×10^{-3}	2.659×10^{-3}	3.79×10^{-4}
FWHM	4.702×10^{-2}	6.0623×10^{-2}	6.615×10^{-3}	7.842×10^{-3}	5.56×10^{-12}
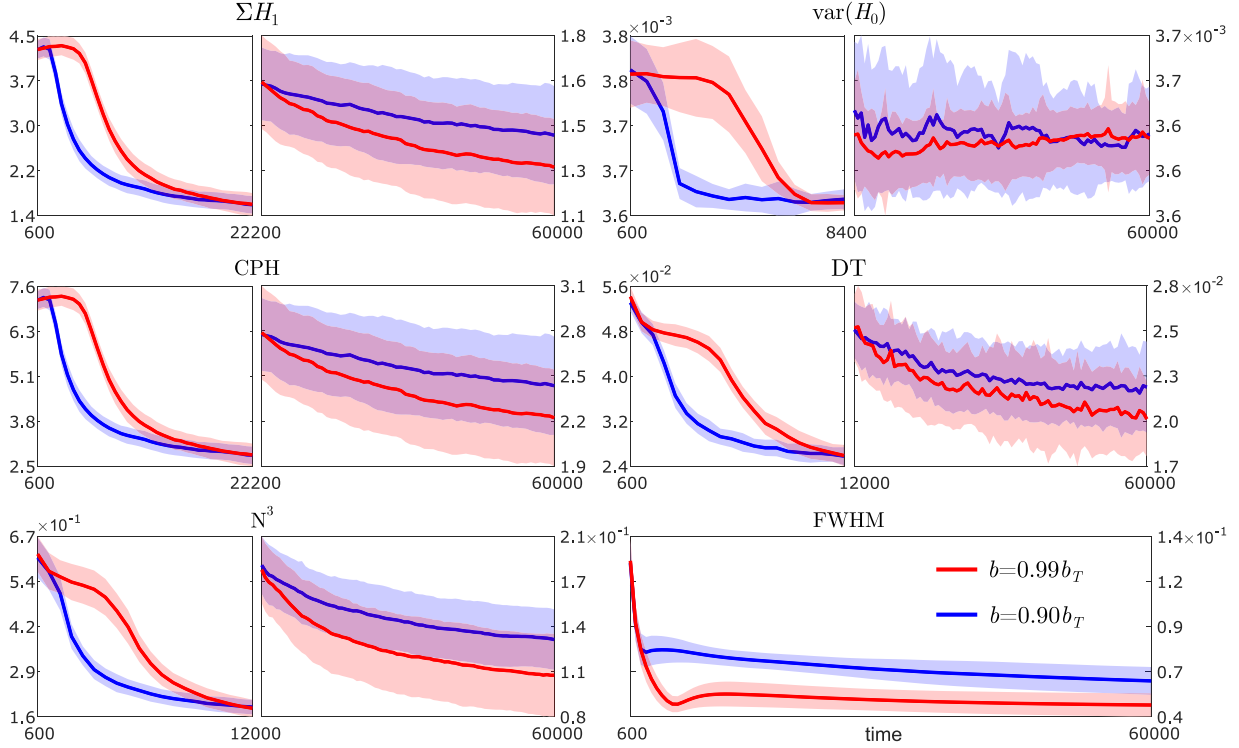
Fig. 9. Measures of hexagonal order for nanodot arrangements averaged over 50 simulations on a 256×256 spatial grid governed by the system (1) with parameters $a = 0.25, c = 1, \nu = 0.75, \lambda = 0, \eta = 10$, and $b = 0.99b_T$ (red) or $0.90b_T$ (blue). Solid lines indicate the averages over all simulations and bands indicate standard deviations. The plots were separated into pairs of temporal regimes when necessary to aid visualization. (For interpretation of the references to colour in this figure legend, the reader is referred to the web version of this article.)

known that the zero mode interacts with active modes through the nonlinearities in Eq. (1), and may play a role in the formation and elimination of defects [6]. Shipman and Bradley [6] found that

$$\frac{dZ}{dt} = \left[\lambda \left(1 - \frac{a}{c} \right) + \frac{2\nu}{a} \left(\frac{a^2 - c^2}{4c^2} \right)^2 \right] \sum_{j=1}^{3} A_j A_j^*$$

$$+ \frac{2\eta}{a} \left(\frac{a^2 - c^2}{4c^2} \right)^3 \mathrm{Re}(A_1 A_2 A_3), \qquad (3)$$

where A_1, A_2 and A_3 are amplitudes of wave vectors that resonate with **0** through the nonlinearities in Eqs. (1). One way to increase the effect of the zero mode is to increase the rate of recession of the surface by increasing ν.

Comparison of surfaces at long times reveals that increasing ν leads to an apparent increase in the average height disparity between defect and defect-free regions of the surface [see Fig. 11(a)]. However, the value of ν has very little effect on the configuration of nanodots. This is reflected in the six measures of hexagonal order, which remain fairly flat as ν increases [see Fig. 11(d)]; that is until an apparent critical value is reached at which point regions with defects appear to be eroded into regions devoid of any patterning at all [see Fig. 11(c)]. This explains the sudden and dramatic changes

in DT and N^3 around $\nu = 1.25$: The variance of the number of neighbors of each nanodot (N^3), and the variability of Delaunay triangulation edge lengths (DT) change suddenly as the number-of-neighbors distribution becomes broad for $\nu > 1.15$. This broadening occurs because the pattern-free depressions introduce large, irregularly-shaped Voronoi cells with many facets.

Notably, $\mathrm{var}(H_0)$, FWHM, and ΣH_1 are less responsive to the kinds of defects introduced by a large value of ν and a high growth rate of the amplitude of the zero mode. A large hole in the lattice may have little effect on the variance in $\mathrm{var}(H_0)$, as the edges connecting nanodots across pattern-free depressed regions are unlikely to be responsible for changing the connectivity of the complex, and at the relevant length scales the complex may already consist of a single connected component. The radially-averaged power spectral density still has a strong peak centered at the characteristic wavelength in the patterned surface, which will be largely unaffected by accentuating the long wavelength morphology of the surface.

Computing ΣH_1 from an H_1 persistence diagram loses much of the geometric content therein. In particular, two persistence diagrams can have the same ΣH_1 even if one consists of a few bars, and the other consists of many small bars. Indeed, Fig. 11**(b)**

$u(x, y, t = 6000)$ $u(x, y, t = 60000)$
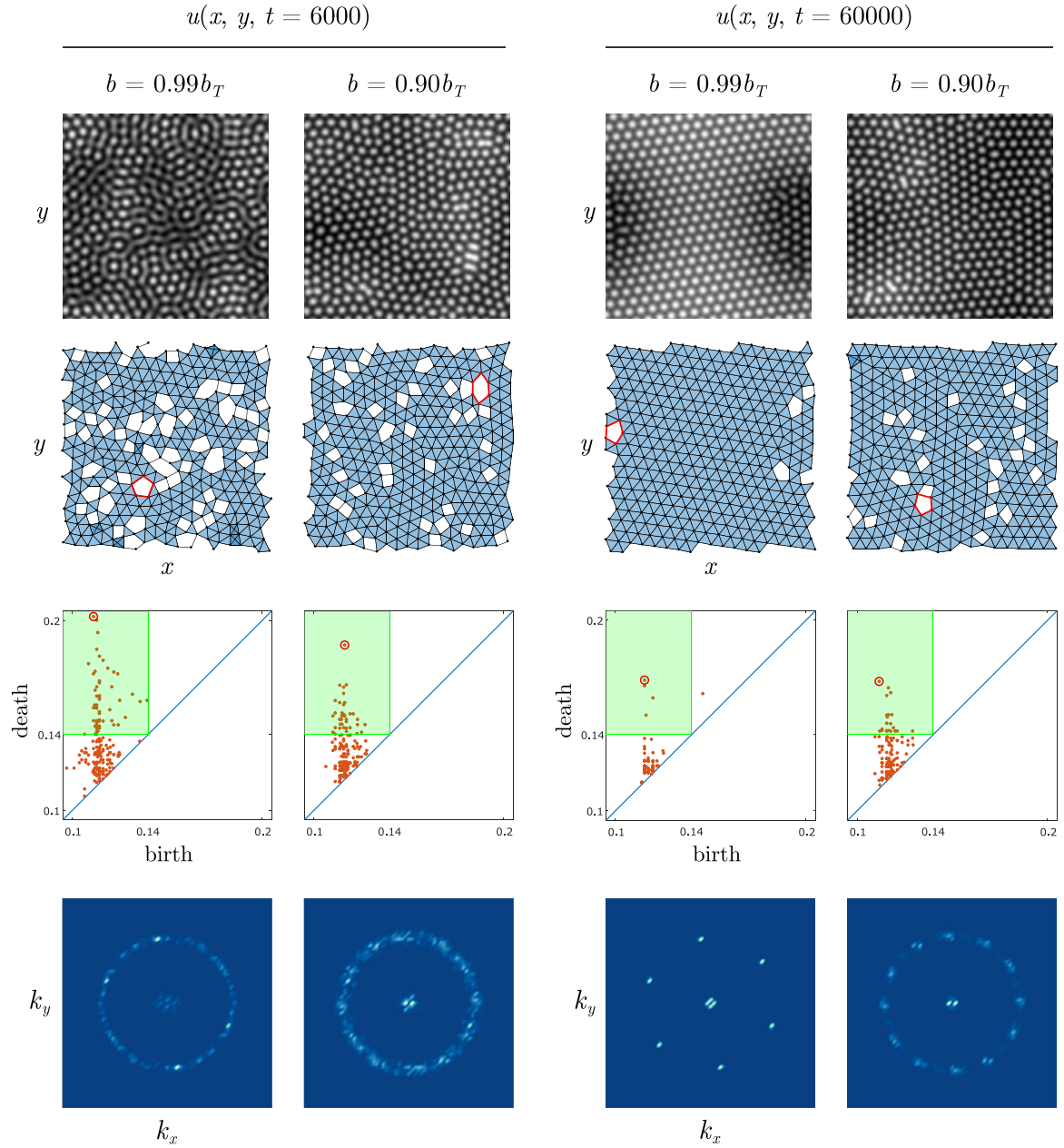
Fig. 10. Snapshots at early and late times of surfaces (row 1), simplicial complexes at connectivity parameter $r = 0.14$ for the nandots extracted from the surfaces (row 2), the corresponding H_1 persistence diagrams (row 3), and 2D power spectral density plots of the (mean centered) surfaces (row 4) for one simulation on a 256×256 spatial grid governed by the system (1) with parameters $a = 0.25$, $c = 1$, $\nu = 0.75$, $\lambda = 0$, $\eta = 10$, $b = 0.99b_T$ (columns 1 and 3) or $0.90b_T$ (columns 2 and 4). Persistence pairs in the green regions of the persistence diagrams correspond to topological holes which were created at a connectivity parameter $r \leq 0.14$, and which are destroyed at a connectivity parameter $r \geq 0.14$ and thus correspond to the topological holes shown in the simplicial complexes (row 2). Holes in the simplicial complex corresponding to the H_1 features with maximum persistence are highlighted in red, and the corresponding persistence pairs are highlighted by red circles. (For interpretation of the references to colour in this figure legend, the reader is referred to the web version of this article.)

and **(c)** show that the relative insensitivity of ΣH_1 to changes in the parameter ν is caused by this tension between the number and significance of topological features: Many small defects accumulate throughout the domain for $\nu = 0.75$. In contrast, the raised patterned regions are almost defect free for $\nu = 1.25$. Instead, the large holes formed for $\nu = 1.25$ by the pattern-free depressions contribute relatively few, but high-persistence pairs to the persistence diagrams. In the example shown in Fig. 11, as ν increases, there is an apparent reduction in the persistence of most of the short-lived topological holes, together with a steady increase in the persistence of a few holes. This is followed by a dramatic increase in the maximum bar length of the H_1 persistence diagram ($\max(H_1)$) by $\nu = 1.25$, as observed in Fig. 11**(b)** and **(d)**.

3.3. Templated patterns

We now use the six measures of order to study how prepatterning the surface prior to ion bombardment affects the strength of hexagonal order achieved after bombarding for a long time. We refer to these prepatterned surfaces as templates, and they correspond to the initial condition of the system (1). The specific functional form of the templates studied in this work is given by

$$u_{\sin,0}(x, y) = 10^{-2} \sin(k_0 x) + \xi(x, y), \tag{4}$$

where $k_0 \equiv 2\pi/\lambda_0$ is the wave number of the template, λ_0 is the wavelength of the initial sinusoid and ξ is small amplitude spatial white noise with amplitude 10^{-4}. A template of this kind could be
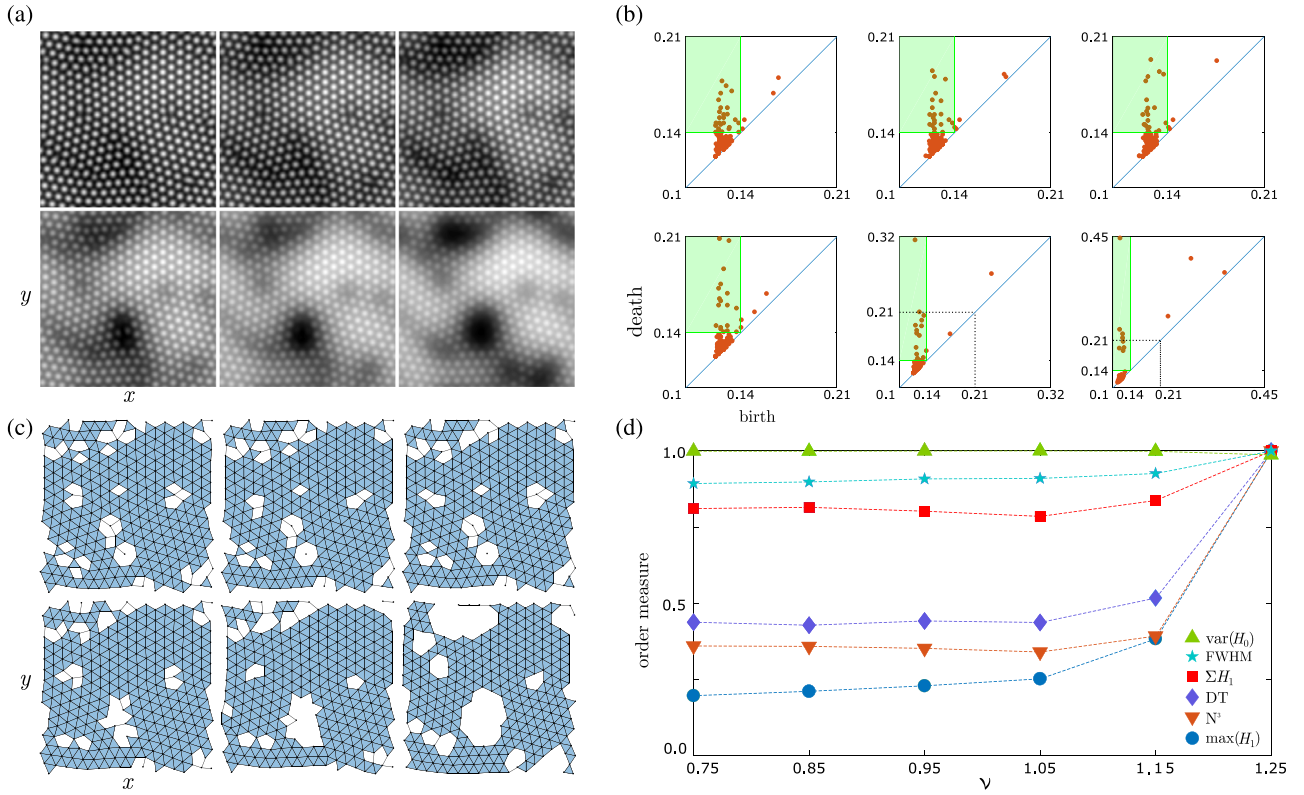
Fig. 11. (a) Snapshots at $t = 60,000$ of surfaces discretized on a 256×256 spatial grid governed by the BS equations (1) with identical initial conditions. Low amplitude spatial white noise initial conditions were used and the parameters were $a = 0.25$, $c = 1$, $\eta = 10$, $\lambda = 0$, and (left to right, top to bottom) $\nu = 0.75, 0.85, 0.95, 1.05, 1.15, 1.25$. **(b)** H_1 persistence diagrams for point clouds of peaks extracted from the surfaces shown in (a). Persistence pairs in the green region of the persistence diagrams correspond to topological holes which were created at a connectivity parameter $r \leq 0.14$, and which are destroyed at a connectivity parameter $r \geq 0.14$. The plotted range of connectivity parameters ($0.1 \leq r \leq 0.21$) for the persistence diagrams of the simulations with $\nu = 0.75$, $\nu = 0.85$, $\nu = 0.95$, and $\nu = 1.05$ are shown by dotted lines in the diagrams of simulations with $\nu = 1.15$ and $\nu = 1.25$ to emphasize the increasing persistence of topological holes with increasing ν. **(c)** Simplicial complexes at connectivity parameter $r = 0.14$ for the arrangements of nanodots extracted from the surfaces. To improve the appearance of the complexes, only those edges and triangles which are both in the simplicial complex and the Delaunay triangulation are shown. **(d)** The measures of order $\text{var}(H_0)$, ΣH_1, DT, N^3 and FWHM averaged over 50 simulations (normalized by the maximum for each measure) plotted versus ν. An additional measure, the maximum bar length $\max(H_1)$ of the H_1 persistence diagram, is also plotted. (For interpretation of the references to colour in this figure legend, the reader is referred to the web version of this article.)

produced in laboratory experiments using standard lithographic methods.

It was shown in Ref. [14] that prepatterning the surface of a binary compound can greatly enhance the overall order of the resulting pattern; however, Pearson et al. only qualitatively demonstrated improvement of order for sinusoidal templates, by comparing the real-space surfaces obtained with or without a prepattern. Here, we extend the analysis of sinusoidal templates to a quantitative study of the degree of order using the measures of order discussed in this paper. For our simulations, we used the domain $0 \leq x, y \leq L$, where $L = 400$ is the width of the spatial domain. We set $N \equiv L/\lambda_0$ for the templated initial conditions and put $N \equiv 0$ for the control case with no templating. In order to respect the periodic boundary conditions, we only used templates with integer values of N. The parameter values used in these simulations of the system (1) were $a = 0.25$, $b = 0.37$, $c = 1$, $\lambda = 0$, $\nu = 1$ and $\eta = 10$. Holding all other parameters fixed, we varied the number of prepatterned wavelengths from $N = 0$ (no template) to $N = 42$. The means and standard deviations of the six measures of order determined from 150 trials of each initial condition are shown in Fig. 12. All simulations were ended at the time $t = 10,000$.

First, we note that, for our choice of parameters, the system (1) has a narrow band of linearly unstable wave vectors centered on the circle of radius k_T. Let $\lambda_T \equiv 2\pi/k_T$ be the linearly selected wavelength of the system. For our choice of parameters, we find that $k_T \simeq 0.61$, and so $\lambda_T \simeq 10.26$. In the qualitative investigations of Ref. [14], it was found that the order at late times was

improved when the template wavelength was sufficiently close to one or two times the linearly selected wavelength. These template wavelengths correspond to $N \simeq 39$ and $N \simeq 20$, respectively. Thus, we expect an effective measure of order to also exhibit these enhancements of order for $N \simeq 39$ and $N \simeq 20$.

Each of the measures of order, except for the N^3 measure, exhibits some degree of enhancement of order for $N = 20$, though they differ in sensitivity to the improvement in order. The topological measures of order all indicate significant improvement in order for $N = 20$, with $\text{var}(H_0)$ indicating the largest improvement in order. The DT and FWHM measures show a lower degree of improvement, whereas the N^3 fails to pick up on any improvement of order.

All of the topological measures indicate significantly increased order for the interval $32 \leq N \leq 40$. The DT and FWHM measures both show improved order for the smaller interval $38 \leq N \leq 40$ and to a lesser extent for the interval $32 \leq N \leq 36$, but curiously show a lack of improved order of $N \simeq 38$. The N^3 actually indicates slightly decreased order for the largest values of N. Qualitative comparison of surface images for $N = 38$ and $N = 0$ clearly shows that the $N = 38$ results have a much higher degree of hexagonal ordering [14]. Therefore, while the DT and FWHM measures may be useful for identifying certain types of disorder, for the patterns resulting from templating, these methods are inferior to the three topological measures for the quantification of hexagonal order.

In all measures except N^3, a higher degree of order was obtained for $N = 40$ than for $N = 39$, even though $N = 39$ yields a
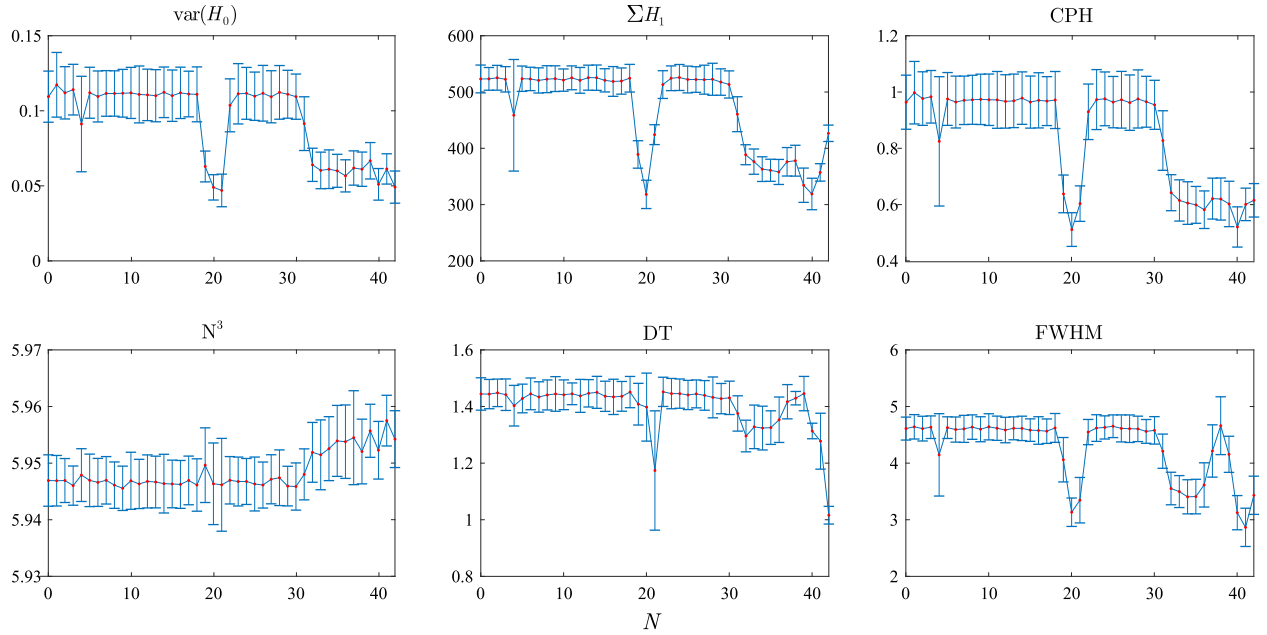
Fig. 12. Each panel shows one of the measures of order for simulations of the system (1) as a function of the number N describing the sinusoidal template (4) used as the initial condition. For $N = 0$, the initial surface was untemplated; otherwise, N denotes number of wavelengths that fit across the spatial domain. The different measures all show that a higher degree of order is achieved near $N = 20$ and beyond $N = 32$, but they differ in their sensitivities to the change in order.

λ_0 that is closer to λ_T. We hypothesize that these increases in disorder are due to the zig-zag instability, which can occur when a pattern's wavelength is slightly longer than the linearly selected wavelength [30]. At early times, the zig-zag instability would have the effect of broadening the Fourier peaks of the $\boldsymbol{k} = \pm k_T \hat{\boldsymbol{x}}$ modes. Due to the quadratic nonlinearity in the system (1), this initial broadening will cause all six peaks which form at $|k| = k_T$ to broaden as well. The FWHM results in Fig. 12 indicate that this broadening of the six Fourier peaks lasts throughout the entire duration of the simulations.

4. Discussion

The six measures of order for nearly hexagonal lattices that we compared in this paper share three practical features. They output a single nonnegative number as the measure of order, are computable in a reasonable amount of time, and can be computed with readily available public tools. Five of the measures can be applied to a set of discrete data points. This includes the class of three topological measures var(H_0), ΣH_1 and CPH, the last two of which have been introduced in this paper. It also includes the geometric-combinatorial measures DT and N^3. To quantify the degree of hexagonal order in surfaces resulting from pattern-forming systems using these five methods, we first extract a set of discrete points from the local maxima of the surface. In contrast, the spectral FWHM measure takes as input the full surface.

Only the topological and geometric-combinatorial measures were therefore applied in the study of Bravais lattices and perturbations of Bravais lattices in Section 2. The measures var(H_0), ΣH_1, and CPH were motivated by observations illustrated in Fig. 6 which show that both var(H_0) and ΣH_1 are equal to zero on one-parameter families of Bravais lattices that intersect only at the (perfect) hexagonal lattice. The linear combination CPH is therefore equal to zero only for the hexagonal lattice. This complementary nature of var(H_0) and ΣH_1 extends to perturbations of Bravais lattices. In the case that only one point is perturbed [Fig. 7], ΣH_1 is more sensitive to small perturbations, whereas var(H_0) is more sensitive to larger perturbations (ΣH_1, for example, changes more rapidly near the center of the hexagon in Fig. 7(b) than close to

the edges of the hexagon while var(H_0) changes very slowly near the center of the hexagon and more rapidly between the center and the edges of the hexagon). A similar comparison plays out for noisy lattices [Fig. 8]: var(H_0) is not a sensitive measure of low levels of noise, but increases more rapidly starting at a noise level of $\mu \simeq 0.4$. In contrast, ΣH_1 increases in a roughly linear fashion, with a slope of approximately 2 until $\mu \simeq 0.4$, but it is approximately constant for larger values of μ. For this reason, the linear combination CPH is a more uniformly increasing function of μ. For noisy lattices, the CPH and DT measures are very similar functions of μ. The N^3 measure as a function of the noise has a similar profile to the var(H_0) measure but is nearly equal to zero until $\mu \simeq 0.3$. Although the DT and CPH measures are similar for the case of noisy lattices, the DT measure shares with the N^3 measure a critical flaw for lattices with a single perturbed point. Observe from Fig. 7 that the N^3 measure is a discontinuous function of the position of the perturbed point and, in fact, does not detect the perturbation unless it is quite large. Although it is less severe, the DT measure also exhibits a jump discontinuity. This means that small changes in the position of the perturbed point can result in a large change in the measure of order by the geometric-combinatorial measures.

Pattern-forming systems can exhibit solitary defects analogous to the case of lattices perturbed at one point as well as disorder analogous to the case of noisy lattices. The fact that the topological measures are sensitive to both of these classes of disorder may be the reason that they measure clearer differences in the degree of order in our study of prepatterned surfaces subject to ion bombardment. For prepatterned surfaces, the spectral measure FWHM shares features with both the topological and geometric-combinatorial measures. Like the topological measures, FWHM shows significant improvement in order for a sinusoidal initial condition with twice the natural wavelength of the pattern ($N = 20$ in Fig. 12). However, only the topological measures show improved order across the entire interval $32 \le N \le 40$ of sinusoidal initial conditions.

The measures of order were also tracked over time as untemplated patterns evolved according to the system (1) for different values of the bifurcation parameter b. For $t = 600$, the time at

which a hexagonal pattern begins to emerge, all of the measures give approximately equal measures of order for the two cases $b = 0.9b_T$ and $b = 0.99b_T$. A short time after $t = 600$, each of the measures indicates a divergence in the degree of order for the two cases. Although the time to divergence is small for all the measures, the topological measures, particularly var(H_0), pick up on the divergence the soonest. From this time to $t \simeq 12,000$, the topological and geometric-combinatorial measures all indicate better order for the case $b = 0.9b_T$ in which the bifurcation parameter is farther from threshold. This is likely due to the fact that the linearly selected Fourier mode corresponding to a ripple with the natural wavelength has a faster growth rate when the bifurcation parameter is farther from threshold, thus allowing the pattern to establish itself sooner. For longer times, the tables turn, and all the measures except for var(H_0) indicate that the pattern is likely to be slightly better ordered for the case $b = 0.99b_T$ (note that the error bars overlap significantly at longer times). The only measure that indicates significantly better order at longer times is the FWHM measure, which defies the trend set by the other five measures and shows better order for the case $b = 0.99b_T$ nearly from the time that the pattern begins to emerge.

The examples of measures of order applied to a pattern-forming system over time provided in this paper suggest that these measures may be useful not only as practical ways of quantifying order, but also as ways of quantifying times at which there a significant change in the character of an evolving pattern. Since parameters affect how the measures change with time, the measures might also be used to help estimate parameter values when comparing experimental data with simulations. This possibility is currently being investigated.

Funding

References

[1] A.V. Getling, Rayleigh-Bénard Convection: Structures and Dynamics, in: Advanced Series in Nonlinear Dynamics, vol. 11, World Scientific Publishing, 1998.
[2] M.D. Cowley, R.E. Rosensweig, J. Fluid Mech. 30 (1967) 671.
[3] S. Facsko, T. Dekorsy, C. Koerdt, C. Trappe, H. Kurz, A. Vogt, H.L. Hartnagel, Formation of ordered nanoscale semiconductor dots by ion sputtering, Science 285 (1999) 1551–1553.
[4] R.M. Bradley, P.D. Shipman, Spontaneous pattern formation induced by ion bombardment of binary compounds, Phys. Rev. Lett. 105 (2010) 145501.
[5] R.M. Bradley, P.D. Shipman, A surface layer of altered composition can play a key role in nanoscale pattern formation induced by ion bombardment, Appl. Surf. Sci. 258 (2012) 4161–4170.
[6] P.D. Shipman, R.M. Bradley, Theory of nanoscale pattern formation induced by normal-incidence ion bombardment of binary compounds, Phys. Rev. B 84 (2011) 085420.
[7] R. Böttger, L. Bischoff, S. Facsko, B. Schmidt, Quantitative analysis of the order of Bi ion induced dot patterns on Ge, Europhys. Lett. 98 (2012) 16009.
[8] G. Carlsson, Topology and data, Bull. Amer. Math. Soc. 46 (2009) 255–308.
[9] S. Ardanza-Trevijano, I. Zuriguel, R. Arévalo, D. Maza, Topological analysis of tapped granular media using persistent homology, Phys. Rev. E 89 (2014) 052212.
[10] M. Kramár, A. Goullet, L. Kondic, K. Mischaikow, Persistence of force networks in compressed granular media, Phys. Rev. E 87 (2013) 042207.
[11] M. Kramár, A. Goullet, L. Kondic, K. Mischaikow, Quantifying force networks in particulate systems, Physica D 283 (2014) 37–55.
[12] M. Kramár, R. Levanger, J. Tithof, B. Suri, M. Xu, M.R. Paul, M.F. Schatz, K. Mischaikow, Analysis of Kolmogorov flow and Rayleigh-Benard convection using persistent homology, Physica D 334 (2016) 82–98.
[13] T. Nakamura, Y. Hiraoka, A. Hirata, E.G. Escolar, Y. Nishiura, Persistent homology and many-body atomic structure for medium-range order in glass, Nanotechnology 26 (2015) 304001.
[14] D.A. Pearson, R.M. Bradley, F.C. Motta, P.D. Shipman, Producing nanodot arrays with improved hexagonal order by patterning surfaces before ion sputtering, Phys. Rev. E 92 (2015) 062401.
[15] H. Edelsbrunner, J. Harer, Computational Topology. An Introduction, Amer. Math. Soc., Providence, 2010.
[16] D. Morozov, Dionysus 2, https://github.com/mrzv/dionysus, GitHub Repository, 2017.
[17] A. Tausz, phom: Persistent Homology in R, https://github.com/cran/phom, GitHub Repository, 2012.
[18] U. Bauer, Ripser, https://github.com/Ripser/ripser, GitHub Repository, 2016.
[19] P. Bendich, J. Harer, R. Bar-On, TDATools, https://gitlab.com/paulbendich/tdatoolstrial, GitHub Repository, 2015.
[20] S. Mátéfi-Tempfli, Mária Mátéfi-Tempfli, Luc Piraux, Characterization of nanopores ordering in anodic alumina, Thin Solid Films 516 (2008) 3735–3740.
[21] L. Bischoff, W. Pilz, B. Schmidt, Amorphous solid foam structures on germanium by heavy ion irradiation, Appl. Phys. A 104 (2011) 1153–1158.
[22] L. Bischoff, K.-H. Heinig, B. Schmidt, S. Facsko, W. Pilz, Self-organization of Ge nanopattern under erosion with heavy Bi monomer and cluster ions, Nucl. Instrum. Methods Phys. Res. B 272 (2012) 198–201.
[23] M. Fritzsche, A. Muecklich, S. Facsko, Nanohole pattern formation on germanium induced by focused ion beam and broad beam Ga+ irradiation, Appl. Phys. Lett. 100 (2012) 223108.
[24] F. Frost, A. Schindler, F. Bigl, Roughness evolution of ion sputtered rotating InP surfaces: Pattern formation and scaling laws, Phys. Rev. Lett. 85 (2000) 4116–4119.
[25] Q. Wei, X. Zhou, B. Joshi, Y. Chen, K.-D. Li, Q. Wei, K. Sun, L. Wang, Self-assembly of ordered semiconductor nanoholes by ion beam sputtering, Adv. Mater. 21 (2009) 2865–2869.
[26] V.B. Shenoy, W.L. Chan, E. Chason, Compositionally modulated ripples induced by sputtering of alloy surfaces, Phys. Rev. Lett. 98 (2007) 256101.
[27] F.C. Motta, P.D. Shipman, R.M. Bradley, Theory of nanoscale pattern formation produced by oblique-incidence ion bombardment of binary compounds, Phys. Rev. B 90 (2014) 085428.
[28] S.M. Cox, P.C. Matthews, Exponential time differencing for stiff systems, J. Comput. Phys. 176 (2002) 430–455.
[29] R.V. Craster, R. Sassi, Spectral Algorithms for Reaction–Diffusion Equations, Università degli studi di Milano, Technical Report 99, 2006.
[30] M. Cross, H. Greenside, Pattern Formation and Dynamics in Nonequilibrium Systems, Cambridge University Press, Cambridge, England, 2009.